Inorg. Chem. **2005**, *44*, 2742–2752

Wheel-Shaped [Mn_{12}] Single-Molecule Magnets

Evan M. Rumberger, Sonali J. Shah, Christopher C. Beedle, Lev N. Zakharov, Arnold L. Rheingold, and David N. Hendrickson*

Department of Chemistry and Biochemistry, University of California at San Diego, La Jolla, California 92093-0358

Received November 29, 2004

The reaction of $[Mn_{12}O_{12}(O_2CCH_3)_{16}(H_2O)_4]\cdot 4H_2O\cdot 2CH_3COOH$ with *n*-methyldiethanol amine (H_2mdea), *n*-ethyldiethanol amine (H_2edea), or *n*-butyldiethanol amine (H_2bdea) leads to the formation of wheel-shaped $Mn^{III}_6Mn^{II}_6$ complexes with the general formula $[Mn_{12}(R)(O_2CCH_3)_{14}]$ (**1**, R = mdea; **2**, R = edea; and **3**, R = bdea). Complex **1** crystallizes in the triclinic space group $P\bar{1}$, whereas complex **3** crystallizes in the monoclinic space group $C_{2/c}$. Complex **1a** has the same molecular structure as complex **1** but crystallizes in the monoclinic space group $P2_{1/n}$. Complex **3a** has the same molecular structure as complex **3** but crystallizes in the triclinic space group $P\bar{1}$. Variable-temperature magnetic susceptibility data collected for complexes **1**, **2**, and **3** indicate that antiferromagnetic exchange interactions are present. The spin ground states of complexes **1**, **2**, and **3** were determined by fitting variable-field magnetization data collected in the 2–5 K temperature range. Fitting of these data yielded the spin ground-state parameters of $S = 8$, $g = 2.0$, and $D = -0.47$ cm^{-1} for complex **1**; $S = 8$, $g = 2.0$, and $D = -0.49$ cm^{-1} for complex **2**; and $S = 8$, $g = 2$, and $D = -0.37$ cm^{-1} for complex **3**. The ac magnetic susceptibility data were measured for complexes **1**, **2**, and **3** at temperatures between 1.8 and 10 K with a 3 G ac field oscillating in the range 50–1000 Hz. Slow kinetics of magnetization reversal relative to the frequency of the oscillating ac field were observed as frequency-dependent out-of-phase peaks for complexes **1**, **2**, and **3**, and it can be concluded that these three complexes are single-molecule magnets.

Introduction

The discovery of single-molecule nanomagnets[1−3] has led to a renewed interest in polynuclear transition metal complexes. Polynuclear manganese single-molecule magnets (SMMs) are by far the most numerous. On the other hand, wheel-shaped clusters of Mn are rare with very few reported examples.[4−7] Wheel-shaped structures occupy a special position among polynuclear complexes for many reasons, not the least of which are the pleasing structural aesthetics.[8] Several recent theoretical studies have indicated that transition metal wheel complexes could be the basis for quantum computation.[9−12] The study and synthesis of antiferromagnetic rings has been pointed out as a significant area of research for nanomagnetism in a recent review paper.[13] Quantum effects associated with these antiferromagnetic rings are expected to be important. Quantum coherence is achieved when a material can tunnel (or "oscillate") between two states, the spin "up" and "down" states, without dissipating energy to or absorbing energy from its environment. A necessary precondition for quantum computing[14,15] with electronic spin states is their coherent evolution under controlled perturbations. The electronic spins in molecular

* To whom correspondence should be addressed. E-mail: dhendrickson@ucsd.edu.

(1) Sessoli, R.; Tsai, H. L.; Schake, A. R.; Wang, S. Y.; Vincent, J. B.; Folting, K.; Gatteschi, D.; Christou, G.; Hendrickson, D. N. *J. Am. Chem. Soc.* **1993**, *115*, 1804.
(2) Sessoli, R.; Gatteschi, D.; Caneschi, A.; Novak, M. A. *Nature* **1993**, *365*, 141.
(3) Caneschi, A.; Gatteschi, D.; Sessoli, R.; Barra, A. L.; Brunel, L. C.; Guillot, M. *J. Am. Chem. Soc.* **1991**, *113*, 5873.
(4) Caneschi, A.; Gatteschi, D.; Laugier, J.; Rey, P.; Sessoli, R.; Zanchini, C. *J. Am. Chem. Soc.* **1988**, *110*, 2795.
(5) Liu, S. X.; Lin, S.; Lin, B. Z.; Lin, C. C.; Huang, J. Q. *Angew. Chem., Int. Ed.* **2001**, *40*, 1084.
(6) Murugesu, M.; Raftery, J.; Wernsdorfer, W.; Christou, G.; Brechin, E. *Inorg. Chem.* **2004**, *43*, 4203.
(7) Tasiopoulos, A. J.; Vinslava, A.; Wernsdorfer, W.; Abboud, K. A.; Christou, G. *Angew. Chem., Int. Ed.* **2004**, *43*, 2117.
(8) Hoffmann, R. *Sci. Am.* **1993**, *268*, 66.
(9) Meier, F.; Levy, J.; Loss, D. *Phys. Rev. B* **2003**, *68*, 134417.
(10) Honecker, A.; Meier, F.; Loss, D.; Normand, B. *Eur. Phys. J. B* **2002**, *27*, 487.
(11) Chiolero, A.; Loss, D. *Physica E* **1997**, *1*, 292.
(12) Meier, F.; Loss, D. *Physica B* **2003**, *329*, 1140.
(13) Gatteschi, D.; Sessoli, R. *Angew. Chem., Int. Ed.* **2003**, *42*, 268.
(14) Leuenberger, M. N.; Loss, D. *Nature* **2001**, *410*, 789.
(15) DiVincenzo, D. P.; Loss, D. *J. Magn. Magn. Mater.* **1999**, *200*, 202.

10.1021/ic048316l CCC: $30.25
Published on Web 03/24/2005

Scheme 1

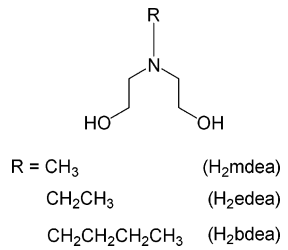

magnets interact with their environment which includes interactions with nuclear spins, lattice vibrations, and other magnetic molecules in the crystal. These interactions tend to destroy tunneling coherence and, for example, reduce the expected quantum oscillations between up and down spin states to an incoherent tunneling transition between these states. The quantum tunneling in an antiferromagnetic ring is predicted to occur coherently.[12] If there is an odd number of antiferromagnetically coupled spin carriers in a ring, the compound will have an uncompensated spin ground state. For example, a compound with 13 antiferromagnetically coupled $S = 1/2$ spin carriers will have a spin ground state of $S = 1/2$. If the remaining uncompensated spin ($S = 1/2$ in this case) is forced to change orientations from a spin up to a spin down ($m_s = -1/2$ to $m_s = 1/2$) then all the other spin carriers in the ring must also reverse their spin in order to maintain the antiferromagnetic exchange interaction. At sufficiently low temperatures, this is expected to occur coherently by a tunneling mechanism. It is also possible to observe quantum effects in even numbered antiferromagnetic rings.[16] If there is a low-lying excited spin state not far in energy from the $S = 0$ ground state, this excited state can be populated by applying a strong magnetic field. At a sufficiently high magnetic field, the excited state will cross over and become lower in energy than the original $S = 0$ ground state. At sufficiently low temperatures, this crossover can occur via quantum tunneling. Gatteschi and Lippard et al. have examined this for an Fe_{10} "ferric wheel".[17] At certain intervals of applied magnetic field, crossovers were observed from the ground state to low-lying excited states.

We recently communicated[18,25] a new wheel-shaped [Mn_{12}] SMM. In the present study, the syntheses and magnetic properties of several [Mn_{12}] complexes are described adding to this family of wheel-shaped Mn-based SMMs. A ligand system (Scheme 1) has been identified that gives wheel-shaped complexes of Mn from different starting materials.

Experimental Section

Synthesis. All manipulations were performed under aerobic conditions. The ligands *n*-ethyldiethanol amine (H_2edea), *n*-methyldiethanol amine (H_2mdea), and *n*-butyldiethanol amine (H_2bdea) were purchased from Aldrich and used without further purification. Crystals of the compounds $[Mn_{12}O_{12}(O_2CCH_3)_{16}(H_2O)_4]\cdot 4H_2O\cdot 2CH_3COOH$ (Mn_{12}Ac) and $[Mn_4O_2(O_2CCH_3)_6(bipy)_2](ClO_4)$ were prepared by standard methods.[19,20]

Table 1. Crystallographic Data for $[Mn_{12}(mdea)_8(O_2CCH_3)_{14}]\cdot 2(CH_3CN)$ (**1**) and $[Mn_{12}(mdea)_8(O_2CCH_3)_{14}]$ (**1a**)

	1	**1a**
formula	$C_{72}H_{136}N_{10}O_{44}Mn_{12}$	$C_{68}H_{130}N_8O_{44}Mn_{12}$
fw	2505.18	2423.08
space group	$P\bar{1}$	$P2_1/n$
a (Å)	13.1038(17)	10.1919(5)
b (Å)	13.2726(18)	15.8827(8)
c (Å)	17.265(2)	31.3229(16)
α (deg)	107.290(2)	−
β (deg)	109.195(2)	98.096(1)
γ (deg)	99.309(2)	−
V (Å^3)	2593.1(6)	5019.9(4)
Z, Z'	1, 0.5	2, 0.5
cryst color, habit	red, block	red, block
cryst size (mm)	0.32 × 0.20 × 0.15	0.19 × 0.18 × 0.15
D_{calc} (g cm^{-3})	1.604	1.603
μ(Mo Kα) (cm^{-1})	14.95	15.41
temp (K)	100(2)	100(2)
diffractometer	Bruker Smart Apex CCD	Bruker Smart Apex CCD
radiation	Mo Kα ($\lambda = 0.71073$ Å)	
reflns measured	21928	32841
reflns independent	11460 [$R_{int} = 0.0228$]	7890 [$R_{int} = 0.0251$]
$R(F)$,[a] $R(\omega F^2)$[b] ($I > 2\sigma(I)$)	0.0365, 0.0908	0.0547, 0.1213
S	1.009	1.268

[a] $R = \sum||F_o| - |F_c||/\sum|F_o|$. [b] $R(\omega F^2) = \{\sum[\omega(F_o^2 - F_c^2)^2]/\sum[\omega(F_o^2)^2]\}^{1/2}$; $\omega = 1/[\sigma^2(F_o^2) + (aP)^2 + bP]$, $P = [2F_c^2 + \max(F_o, 0)]/3$.

[$Mn_{12}(mdea)_8(O_2CCH_3)_{14}$] (complexes [$Mn_{12}(mdea)_8(O_2CCH_3)_{14}]\cdot CH_3CN$ (1) and [$Mn_{12}(mdea)_8(O_2CCH_3)_{14}$] (1a)). Method (a). A CH_2Cl_2 (25 mL) solution of H_2mdea (0.462 g, 3.88 mmol) was added dropwise to a CH_2Cl_2 (100 mL) slurry of Mn_{12}Ac (2.0 g, 0.971 mmol). The slurry was stirred overnight, during which time the Mn_{12}Ac slowly dissolved forming a black/brown solution. The undissolved Mn_{12}Ac was removed by filtration, and the filtrate was evaporated by vacuum distillation yielding a brown oil. The oil was washed with 30 mL of diethyl ether to remove the excess ligand. The oil was then dissolved in 30 mL of acetonitrile and left undisturbed. After 30 min, crystals of complex **1** started to precipitate. Yield: 0.160 g (7%, based on Mn). Anal. Calcd (found) for $C_{68}H_{130}Mn_{12}N_8O_{44}$: C, 33.70 (33.96); H, 5.40 (5.00); N, 4.62 (4.64). Selected IR data (KBr): 3440 (m,br), 3143 (m,br), 2848 (m), 1581 (s), 1400 (s), 1334 (m), 1079 (m), 663 (w), 522 cm^{-1} (w). Crystals of complex **1** were grown by allowing diethyl ether vapors to slowly diffuse into an acetonitrile solution of complex **1**. Red rod-shaped crystals of the second form, complex **1a**, were grown by very slowly adding 30 mL of acetonitrile to the oil collected from the vacuum distillation step.

Method (b). Solid $[Mn_4O_2(O_2CCH_3)_7(bpy)_2](ClO_4)$ (0.5 g, 0.442 mmol) was added to CH_2Cl_2 (30 mL). After being stirred for 1 h, the brown/red solution was filtered to remove undissolved $[Mn_4O_2(O_2CMe)_7(bpy)_2](ClO_4)$. H_2mdea (0.239 g, 1.77 mmol) dissolved in CH_2Cl_2 (10 mL) was added dropwise over a 5 min period to the filtrate. The resulting red solution was stirred for 30 min. The solution was allowed to stand undisturbed for 3 days, after which a brown/red precipitate formed (complex **1**). Complex **1** was collected via vacuum filtration and washed with three successive 30 mL treatments of diethyl ether. Crystals of **1** were grown by layering a 50 mL CH_3CN solution with a 50 mL 1:1 mixture of

(16) Waldmann, O. *Europhys. Lett.* **2002**, *60*, 302.
(17) Taft, K. L.; Delfs, C. D.; Papaefthymiou, G. C.; Foner, S.; Gatteschi, D.; Lippard, S. J. *J. Am. Chem. Soc.* **1994**, *116*, 823.
(18) Rumberger, E. M.; Zakharov, L. N.; Rheingold, A. L.; Hendrickson, D. N. *Inorg. Chem.* **2004**, *43*, 6531.
(19) Lis, T. *Acta Crystallogr., Sect. B: Struct. Sci.* **1980**, *36*, 2042.
(20) Vincent, J. B.; Christmas, C.; Chang, H. R.; Li, Q. Y.; Boyd, P. D. W.; Huffman, J. C.; Hendrickson, D. N.; Christou, G. *J. Am. Chem. Soc.* **1989**, *111*, 2086.

Table 2. Crystallographic Data for $[Mn_{12}(bdea)_8(O_2CCH_3)_{14}]\cdot 3CH_3CN$ (**3**) and $[Mn_{12}(bdea)_8(O_2CCH_3)_{14}]$ (**3a**)

	3	**3a**
formula	$C_{98}H_{187}Mn_{12}N_{11}O_{44}$	$C_{92}H_{178}Mn_{12}N_8O_{44}$
fw	2882.87	2759.70
space group	*C*2/*c*	$P\bar{1}$
a (Å)	26.0196(17)	14.5942(13)
b (Å)	20.6862(14)	15.7162(14)
c (Å)	24.1927(16)	16.5559(15)
α (deg)	90	117.582(1)
β (deg)	91.064(1)	96.440(1)
γ (deg)	90	108.629(1)
V (Å^3)	13019.4(15)	3032.7(5)
Z, *Z*′	4, 0.5	1, 0.5
cryst color, habit	brown, plate	brown, needle
cryst size (mm)	0.15 × 0.14 × 0.03	0.32 × 0.08 × 0.03
D_{calc} (mg m^{-3})	1.471	1.511
μ(Mo Kα) (cm^{-1})	12.02	12.86
temp (K)	100(2)	100(2)
diffractometer	Bruker Smart Apex CCD	Bruker Smart Apex CCD
radiation	Mo Kα (λ = 0.71073 Å)	
reflns measured	56454	26100
reflns independent	14795 [R_{int} = 0.0438]	13114 [R_{int} = 0.0401]
$R(F)$,[a] $R(\omega F^2)$[b] ($I > 2\sigma(I)$)	0.0428, 0.0989	0.0475, 0.1000

[a] $R = \sum||F_o| - |F_c||/\sum|F_o|$. [b] $R(\omega F^2) = \{\sum[\omega(F_o^2 - F_c^2)^2]/\sum[\omega(F_o^2)^2]\}^{1/2}$; $\omega = 1/[\sigma^2(F_o^2) + (aP)^2 + bP]$, $P = [2F_c^2 + \max(F_o, 0)]/3$.

Table 3. Selected Interatomic Distances (Å) for $[Mn_{12}(mdea)_8(O_2CCH_3)_{14}]\cdot 2CH_3CN$ (**1**)

Mn(1)−O(16)#1	2.1107(18)	Mn(3)−Mn(4)	3.1695(7)
Mn(1)−O(18)#1	2.1430(18)	Mn(4)−O(8)	1.8819(17)
Mn(1)−O(3)	2.1719(18)	Mn(4)−O(11)	1.9066(17)
Mn(1)−O(20)#1	2.1990(18)	Mn(4)−O(12)	1.9170(17)
Mn(1)−O(1)	2.2008(18)	Mn(4)−O(13)	1.9498(18)
Mn(1)−O(5)	2.2225(17)	Mn(4)−O(10)	2.2545(18)
Mn(1)−Mn(2)	3.1980(7)	Mn(4)−N(3)	2.302(2)
Mn(2)−O(7)	1.8890(17)	Mn(4)−Mn(5)	3.1499(6)
Mn(2)−O(4)	1.9015(17)	Mn(5)−O(12)	2.0972(18)
Mn(2)−O(3)	1.9290(17)	Mn(5)−O(21)	2.1199(19)
Mn(2)−O(2)	1.9848(17)	Mn(5)−O(14)	2.1593(18)
Mn(2)−O(5)	2.1989(17)	Mn(5)−O(17)	2.1827(17)
Mn(2)−N(1)	2.311(2)	Mn(5)−O(10)	2.1942(17)
Mn(2)−Mn(3)	3.1824(6)	Mn(5)−O(15)	2.2502(18)
Mn(3)−O(4)	2.2040(18)	Mn(5)−Mn(6)	3.2065(6)
Mn(3)−O(8)	2.2106(18)	Mn(6)−O(17)	1.9006(18)
Mn(3)−O(6)	2.2335(18)	Mn(6)−O(18)	1.9137(18)
Mn(3)−O(11)	2.2346(17)	Mn(6)−O(19)	1.9389(18)
Mn(3)−O(9)	2.2459(18)	Mn(6)−O(22)	1.9761(18)
Mn(3)−O(7)	2.2878(17)	Mn(6)−O(15)	2.1768(17)
Mn(3)−N(2)	2.419(2)	Mn(6)−N(4)	2.334(2)

diethyl ether and hexanes. Elemental analysis and FT-IR spectral data agree with the data collected for crystals prepared via method (a) for complex **1**. Crystals prepared by method (b) have the same X-ray structure as complex **1**. Yield: 0.0384 g (3% based on Mn).

$[Mn_{12}(edea)_8(O_2CCH_3)_{14}]$ (complex 2). Method (a). Complex **2** was prepared in a fashion analogous to that used for complex **1** (method (a)) except that H_2edea (0.516 g, 3.88 mmol) was used instead of H_2mdea. Yield: 0.202 g (8%, based on Mn). Anal. Calcd (found) for $C_{76}H_{146}Mn_{12}N_8O_{44}$: C, 36.00 (36.65); H, 5.80 (5.35); N, 4.41 (4.35). Selected IR data (KBr): 3421 (s,br), 1560 (s), 1403 (s), 1342 (w), 1078 (m), 661 (w), 458 cm^{-1} (w).

Method (b). Complex **2** was prepared in a procedure analogous to that used to prepare complex **1** (method (b)) except that the precipitation of **2** immediately followed the addition of H_2edea (0.233 g, 1.77 mmol) to the CH_2Cl_2 solution (30 mL). The FT-IR spectra of crystals prepared by method (b) agree with the data collected for crystals prepared using method (a) for complex **2**. The yield of complex **2** formed by method (b) was very small.

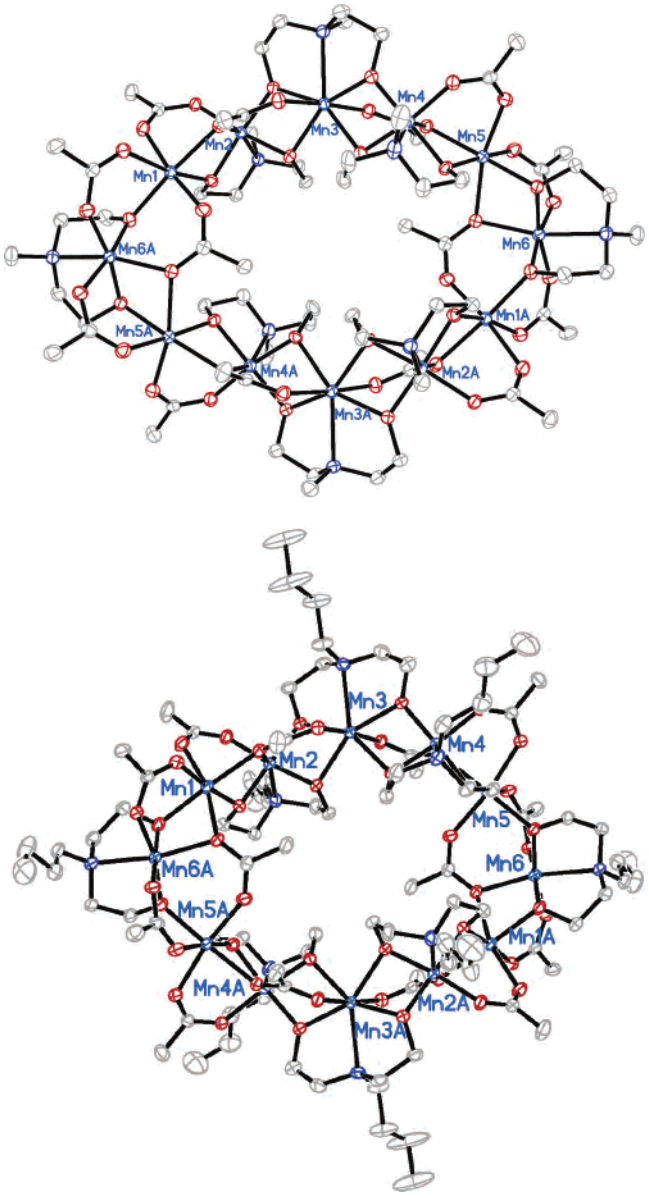

Figure 1. ORTEP diagrams of complexes **1** (upper) and **3** (lower) displayed at the 50% probability level. Hydrogen atoms and solvate molecules have been omitted for clarity.

$[Mn_{12}(bdea)_8(O_2CCH_3)_{14}]$ (complexes $[Mn_{12}(mdea)_8(O_2CCH_3)_{14}]\cdot 3CH_3CN$ (3) and $[Mn_{12}(bdea)_8(O2CCH_3)_{14}]$ (3a)). Complex **3a** was prepared in a manner analogous to that used for complex **1** except that H_2bdea was used (0.626 g, 3.88 mmol) instead of H_2mdea. Fifty milliliters of acetonitrile was added to the oil obtained after the vacuum distillation step. This solution was filtered, and the filtrate was allowed to slowly evaporate. After 2 days, 20 mL of the acetonitrile had evaporated and a crystal had formed on the side of the flask. The yield was exceptionally low; only one crystal was obtained after evaporating the filtrate. This crystal was found to be suitable for X-ray crystallography studies.

In light of the exceptionally low yield, alternate synthetic methods were sought. The yield was improved by doubling the molar equivalents of the ligand H_2bdea relative to the Mn_{12}Ac. A CH_2Cl_2 (25 mL) solution of H_2bdea (1.252 g, 7.76 mmol) was added dropwise to a CH_2Cl_2 (100 mL) slurry of Mn_{12}Ac (2.0 g, 0.971 mmol). The slurry was allowed to stir for 2 days during which the Mn_{12}Ac dissolved and formed a brown solution. The undissolved Mn_{12}Ac was removed by filtration. A greenish-brown insoluble

Table 4. Selected Interatomic Angles (deg) for $[Mn_{12}(mdea)_8(O_2CCH_3)_{14}]\cdot 2CH_3CN$ (**1**)

O(16)#1−Mn(1)−O(18)#1	92.96(7)	O(8)−Mn(4)−O(11)	83.01(7)	O(18)−Mn(6)−N(4)	81.45(7)
O(16)#1−Mn(1)−O(3)	97.25(7)	O(8)−Mn(4)−O(12)	178.39(8)	O(19)−Mn(6)−N(4)	93.40(8)
O(18)#1−Mn(1)−O(3)	96.90(7)	O(11)−Mn(4)−O(12)	95.80(8)	O(22)−Mn(6)−N(4)	92.92(8)
O(16)#1−Mn(1)−O(20)#1	93.87(7)	O(8)−Mn(4)−O(13)	89.26(8)	O(15)−Mn(6)−N(4)	161.22(7)
O(18)#1−Mn(1)−O(20)#1	87.58(7)	O(11)−Mn(4)−O(13)	171.61(8)	C(1)−O(1)−Mn(1)	130.15(16)
O(3)−Mn(1)−O(20)#1	167.77(7)	O(12)−Mn(4)−O(13)	91.99(7)	C(1)−O(2)−Mn(2)	128.70(16)
O(16)#1−Mn(1)−O(1)	172.41(7)	O(8)−Mn(4)−O(10)	99.81(7)	C(3)−O(3)−Mn(2)	113.49(14)
O(18)#1−Mn(1)−O(1)	94.54(7)	O(11)−Mn(4)−O(10)	87.27(7)	C(3)−O(3)−Mn(1)	126.54(14)
O(3)−Mn(1)−O(1)	83.02(6)	O(12)−Mn(4)−O(10)	79.02(7)	Mn(2)−O(3)−Mn(1)	102.33(8)
O(20)#1−Mn(1)−O(1)	85.29(7)	O(13)−Mn(4)−O(10)	97.29(7)	C(6)−O(4)−Mn(2)	115.86(15)
O(16)#1−Mn(1)−O(5)	86.13(7)	O(8)−Mn(4)−N(3)	102.29(8)	C(6)−O(4)−Mn(3)	121.08(15)
O(18)#1−Mn(1)−O(5)	173.86(7)	O(11)−Mn(4)−N(3)	82.08(8)	Mn(2)−O(4)−Mn(3)	101.38(7)
O(3)−Mn(1)−O(5)	77.21(6)	O(12)−Mn(4)−N(3)	78.59(8)	C(8)−O(5)−Mn(2)	123.44(15)
O(20)#1−Mn(1)−O(5)	98.54(7)	O(13)−Mn(4)−N(3)	96.47(8)	C(8)−O(5)−Mn(1)	134.07(15)
O(1)−Mn(1)−O(5)	86.54(6)	O(10)−Mn(4)−N(3)	154.03(8)	Mn(2)−O(5)−Mn(1)	92.65(7)
O(7)−Mn(2)−O(4)	82.67(7)	C(4)−N(1)−Mn(2)	105.37(15)	C(8)−O(6)−Mn(3)	134.85(17)
O(7)−Mn(2)−O(3)	175.29(8)	C(11)−N(2)−Mn(3)	104.68(15)	C(10)−O(7)−Mn(2)	128.89(15)
O(4)−Mn(2)−O(3)	94.60(7)	C(12)−N(2)−Mn(3)	106.30(15)	C(10)−O(7)−Mn(3)	119.97(15)
O(7)−Mn(2)−O(2)	91.58(7)	C(14)−N(2)−Mn(3)	111.99(16)	Mn(2)−O(7)−Mn(3)	98.82(7)
O(4)−Mn(2)−O(2)	172.75(7)	C(21)−N(3)−Mn(4)	113.34(18)	C(13)−O(8)−Mn(4)	127.15(15)
O(3)−Mn(2)−O(2)	90.82(7)	C(18)−N(3)−Mn(4)	100.20(15)	C(13)−O(8)−Mn(3)	120.58(15)
O(7)−Mn(2)−O(5)	100.93(7)	C(19)−N(3)−Mn(4)	105.80(16)	Mn(4)−O(8)−Mn(3)	101.21(8)
O(4)−Mn(2)−O(5)	92.53(7)	C(30)−N(4)−Mn(6)	113.50(17)	C(15)−O(9)−Mn(3)	132.49(16)
O(3)−Mn(2)−O(5)	82.99(7)	C(28)−N(4)−Mn(6)	100.43(15)	C(15)−O(10)−Mn(5)	139.76(16)
O(2)−Mn(2)−O(5)	92.90(7)	C(27)−N(4)−Mn(6)	104.80(15)	C(15)−O(10)−Mn(4)	125.43(15)
O(7)−Mn(2)−N(1)	96.26(8)	O(12)−Mn(5)−O(21)	173.86(7)	Mn(5)−O(10)−Mn(4)	90.14(6)
O(4)−Mn(2)−N(1)	81.89(7)	O(12)−Mn(5)−O(14)	91.50(7)	C(17)−O(11)−Mn(4)	116.58(16)
O(3)−Mn(2)−N(1)	79.52(7)	O(21)−Mn(5)−O(14)	94.23(7)	C(17)−O(11)−Mn(3)	121.47(15)
O(2)−Mn(2)−N(1)	94.40(7)	O(12)−Mn(5)−O(17)	94.01(7)	Mn(4)−O(11)−Mn(3)	99.57(7)
O(5)−Mn(2)−N(1)	161.11(7)	O(21)−Mn(5)−O(17)	88.31(7)	C(20)−O(12)−Mn(4)	114.68(16)
O(4)−Mn(3)−O(8)	148.68(6)	O(14)−Mn(5)−O(17)	88.83(7)	C(20)−O(12)−Mn(5)	123.79(15)
O(4)−Mn(3)−O(6)	85.27(7)	O(12)−Mn(5)−O(10)	76.80(6)	Mn(4)−O(12)−Mn(5)	103.29(8)
O(8)−Mn(3)−O(6)	88.16(6)	O(21)−Mn(5)−O(10)	101.19(7)	C(22)−O(13)−Mn(4)	130.71(17)
O(4)−Mn(3)−O(11)	80.90(6)	O(14)−Mn(5)−O(10)	87.85(7)	C(22)−O(14)−Mn(5)	127.77(17)
O(8)−Mn(3)−O(11)	68.77(6)	O(17)−Mn(5)−O(10)	170.14(7)	C(24)−O(15)−Mn(6)	128.33(16)
O(6)−Mn(3)−O(11)	92.21(7)	O(12)−Mn(5)−O(15)	89.21(7)	C(24)−O(15)−Mn(5)	128.46(16)
O(4)−Mn(3)−O(9)	93.17(7)	O(21)−Mn(5)−O(15)	85.89(7)	Mn(6)−O(15)−Mn(5)	92.81(7)
O(8)−Mn(3)−O(9)	91.18(6)	O(14)−Mn(5)−O(15)	163.89(7)	C(24)−O(16)−Mn(1)#1	137.71(17)
O(6)−Mn(3)−O(9)	175.79(7)	O(17)−Mn(5)−O(15)	75.07(6)	C(26)−O(17)−Mn(6)	114.68(15)
O(11)−Mn(3)−O(9)	83.69(6)	O(10)−Mn(5)−O(15)	107.96(6)	C(26)−O(17)−Mn(5)	120.76(15)
O(4)−Mn(3)−O(7)	67.72(6)	O(17)−Mn(6)−O(18)	94.24(8)	Mn(6)−O(17)−Mn(5)	103.27(8)
O(8)−Mn(3)−O(7)	142.55(6)	O(17)−Mn(6)−O(19)	169.69(8)	C(29)−O(18)−Mn(6)	116.12(15)
O(6)−Mn(3)−O(7)	87.41(6)	O(18)−Mn(6)−O(19)	91.38(8)	C(29)−O(18)−Mn(1)#1	122.68(15)
O(11)−Mn(3)−O(7)	148.55(6)	O(17)−Mn(6)−O(22)	90.02(8)	Mn(6)−O(18)−Mn(1)#1	117.63(8)
O(9)−Mn(3)−O(7)	95.62(6)	O(18)−Mn(6)−O(22)	172.14(7)	C(31)−O(19)−Mn(6)	138.15(17)
O(4)−Mn(3)−N(2)	138.36(7)	O(19)−Mn(6)−O(22)	83.45(7)	C(31)−O(20)−Mn(1)#1	128.87(17)
O(8)−Mn(3)−N(2)	72.38(7)	O(17)−Mn(6)−O(15)	82.68(7)	C(33)−O(21)−Mn(5)	128.04(17)
O(6)−Mn(3)−N(2)	92.06(7)	O(18)−Mn(6)−O(15)	96.22(7)	C(33)−O(22)−Mn(6)	131.54(17)
O(11)−Mn(3)−N(2)	140.73(7)	O(19)−Mn(6)−O(15)	105.31(7)	C(7)−N(1)−Mn(2)	111.84(16)
O(9)−Mn(3)−N(2)	91.70(7)	O(22)−Mn(6)−O(15)	90.87(7)	C(5)−N(1)−Mn(2)	100.53(15)
O(7)−Mn(3)−N(2)	70.65(7)	O(17)−Mn(6)−N(4)	78.93(7)		

precipitate was also removed by filtration and discarded. The filtrate was evaporated by vacuum distillation to 5−10 mL. Then 50 mL of acetonitrile was added to this solution. After a final filtration, crystals immediately precipitated in the filtration flask. Yield: 0.966 g (48.3% based on Mn). Anal. Calcd (found) for $C_{92}H_{178}Mn_{12}N_8O_{44}$: C, 40.00 (38.77); H, 6.50 (5.09); N, 4.06 (4.09). Selected IR data (KBr): 3434 (s,br), 1582 (s), 1401 (s), 1338 (w), 1087 (m), 661 (w), 577 (w), 498 cm^{-1} (w).

Physical Measurements. FT-IR spectra were collected using a Thermo-Nicolet Avatar series spectrometer. Elemental analyses were performed by Prevalere Life Sciences (Whitesboro, NY). The ac and dc magnetic susceptibility data were collected with Quantum Design MPMS magnetometers equipped with 1.0 and 5.5 T magnets, respectively. Microcrystalline samples were restrained with eicosane to prevent torquing of the crystallites. Pascal's constants were employed to adjust the observed magnetic susceptibilities with a diamagnetic correction. All NMR spectra were recorded at room temperature (20 °C) in d_3-chloroform solutions on Varian spectrometers operating at 300 MHz (^{1}H NMR) and referenced to residual solvent peaks unless otherwise noted.

X-ray Crystallography. Diffraction intensity data were collected at 100 K with a Bruker Smart Apex CCD diffractometer. Crystal data, data collection, and refinement parameters for complexes **1** and **1a** and complexes **3** and **3a** are given in Tables 1 and 2, respectively. The space groups were chosen on the basis of intensity statistics (**1** and **3a**), systematic absences (**1a**), and systematic absences and intensity statistics (**3**). The structures were solved employing direct methods, completed by subsequent difference Fourier syntheses, and refined by full matrix least-squares procedures on F^2. SADABS[21] absorption corrections were applied to all data ($T_{min}/T_{max} = 0.774$ (**1**), 0.729 (**1a**), 0.896 (**3**), and 0.599 (**3a**)). Complexes **1** and **3** cocrystallize with acetonitrile solvate molecules. There are two CH_3CN solvate molecules per $[Mn_{12}]$ wheel in complex **1** and three CH_3CN per $[Mn_{12}]$ wheel in complex **3**. One CH_3CN solvate molecule in **3** is highly disordered around a center of symmetry and was treated by the SQUEEZE program.[22] The

(21) Sheldrick, G. M. *SADABS, Bruker/Siemens Area Detector Absorption Correction Program*, version 2.01; Bruker AXS: Madison, WI, 1998.
(22) Van der Sluis, P.; Spek, A. L. *Acta Crystallogr., Sect. A* **1990**, *46*, 194.

Table 5. Selected Interatomic Distances (Å) for $[Mn_{12}(bdea)_8(O_2CCH_3)_{14}]\cdot 3CH_3CN$ (**3**)

Mn(1)−O(3)	2.1112(19)	Mn(3)−N(2)	2.463(2)
Mn(1)−O(20)#1	2.1445(19)	Mn(3)−Mn(4)	3.1678(6)
Mn(1)−O(1)	2.1570(18)	Mn(4)−O(8)	1.8890(18)
Mn(1)−O(18)#1	2.1919(19)	Mn(4)−O(11)	1.8893(18)
Mn(1)−O(16)#1	2.1976(17)	Mn(4)−O(12)	1.9141(17)
Mn(1)−O(5)	2.2079(18)	Mn(4)−O(13)	1.9681(18)
Mn(1)−Mn(2)	3.1802(6)	Mn(4)−O(10)	2.2093(18)
Mn(1)−Mn(6)#1	3.2025(6)	Mn(4)−N(3)	2.384(2)
Mn(2)−O(7)	1.8761(18)	Mn(4)−Mn(5)	3.1847(6)
Mn(2)−O(4)	1.8954(17)	Mn(5)−O(15)	2.1388(19)
Mn(2)−O(3)	1.9237(18)	Mn(5)−O(12)	2.1433(18)
Mn(2)−O(2)	1.9464(17)	Mn(5)−O(17)	2.1520(17)
Mn(2)−O(5)	2.2618(18)	Mn(5)−O(21)	2.1616(18)
Mn(2)−N(1)	2.331(2)	Mn(5)−O(14)	2.2117(18)
Mn(2)−Mn(3)	3.1565(6)	Mn(5)−O(10)	2.2306(17)
Mn(3)−O(7)	2.2046(18)	Mn(6)−O(17)	1.9014(17)
Mn(3)−O(6)	2.2064(18)	Mn(6)−O(18)	1.9031(18)
Mn(3)−O(11)	2.2102(17)	Mn(6)−O(22)	1.9438(18)
Mn(3)−O(8)	2.2291(18)	Mn(6)−O(19)	1.9675(18)
Mn(3)−O(9)	2.2347(18)	Mn(6)−O(16)	2.2071(18)
Mn(3)−O(4)	2.2583(18)	Mn(6)−N(4)	2.375(2)

Table 6. Selected Interatomic Angles (deg) for $[Mn_{12}(bdea)_8(O_2CCH_3)_{14}]\cdot 3CH_3CN$ (**3**)

O(3)−Mn(1)−O(20)#1	174.28(7)	O(11)−Mn(3)−O(9)	84.38(7)
O(3)−Mn(1)−O(1)	90.44(7)	O(8)−Mn(3)−O(9)	87.98(7)
O(20)#1−Mn(1)−O(1)	89.01(7)	O(7)−Mn(3)−O(4)	67.77(6)
O(3)−Mn(1)−O(18)#1	94.76(7)	O(6)−Mn(3)−O(4)	84.02(7)
O(20)#1−Mn(1)−O(18)#1	90.93(7)	O(11)−Mn(3)−O(4)	81.36(6)
O(1)−Mn(1)−O(18)#1	89.89(7)	O(8)−Mn(3)−O(4)	149.51(7)
O(3)−Mn(1)−O(16)#1	93.76(7)	O(9)−Mn(3)−O(4)	92.22(7)
O(20)#1−Mn(1)−O(16)#1	88.31(7)	O(7)−Mn(3)−N(2)	71.62(7)
O(1)−Mn(1)−O(16)#1	163.99(7)	O(6)−Mn(3)−N(2)	91.24(7)
O(18)#1−Mn(1)−O(16)#1	74.38(6)	O(11)−Mn(3)−N(2)	139.96(7)
O(3)−Mn(1)−O(5)	76.35(7)	O(8)−Mn(3)−N(2)	71.66(7)
O(20)#1−Mn(1)−O(5)	97.93(7)	O(9)−Mn(3)−N(2)	93.47(7)
O(1)−Mn(1)−O(5)	87.56(7)	O(4)−Mn(3)−N(2)	138.65(7)
O(18)#1−Mn(1)−O(5)	170.73(7)	O(8)−Mn(4)−O(11)	82.56(8)
O(16)#1−Mn(1)−O(5)	108.44(7)	O(8)−Mn(4)−O(12)	174.54(8)
O(7)−Mn(2)−O(4)	82.57(8)	O(11)−Mn(4)−O(12)	93.56(8)
O(7)−Mn(2)−O(3)	178.15(8)	O(8)−Mn(4)−O(13)	91.77(7)
O(4)−Mn(2)−O(3)	95.65(8)	O(11)−Mn(4)−O(13)	174.02(7)
O(7)−Mn(2)−O(2)	90.02(8)	O(12)−Mn(4)−O(13)	92.23(7)
O(4)−Mn(2)−O(2)	171.52(8)	O(8)−Mn(4)−O(10)	100.59(7)
O(3)−Mn(2)−O(2)	91.72(8)	O(11)−Mn(4)−O(10)	90.08(7)
O(7)−Mn(2)−O(5)	101.61(7)	O(12)−Mn(4)−O(10)	83.20(7)
O(4)−Mn(2)−O(5)	89.23(7)	O(13)−Mn(4)−O(10)	89.10(7)
O(3)−Mn(2)−O(5)	78.84(7)	O(8)−Mn(4)−N(3)	97.93(8)
O(2)−Mn(2)−O(5)	96.32(7)	O(11)−Mn(4)−N(3)	81.84(8)
O(7)−Mn(2)−N(1)	99.97(8)	O(12)−Mn(4)−N(3)	77.65(7)
O(4)−Mn(2)−N(1)	82.56(8)	O(13)−Mn(4)−N(3)	100.90(8)
O(3)−Mn(2)−N(1)	79.24(8)	O(10)−Mn(4)−N(3)	158.65(7)
O(2)−Mn(2)−N(1)	94.74(8)	O(17)−Mn(6)−O(18)	95.78(8)
O(5)−Mn(2)−N(1)	155.68(8)	O(17)−Mn(6)−O(22)	91.08(7)
O(7)−Mn(3)−O(6)	93.70(7)	O(18)−Mn(6)−O(22)	173.01(8)
O(7)−Mn(3)−O(11)	147.71(7)	O(17)−Mn(6)−O(19)	166.48(8)
O(6)−Mn(3)−O(11)	92.21(7)	O(18)−Mn(6)−O(19)	90.26(8)
O(7)−Mn(3)−O(8)	142.62(7)	O(22)−Mn(6)−O(19)	83.33(7)
O(6)−Mn(3)−O(8)	93.81(7)	O(17)−Mn(6)−O(16)	99.00(7)
O(11)−Mn(3)−O(8)	68.31(6)	O(18)−Mn(6)−O(16)	80.04(7)
O(7)−Mn(3)−O(9)	87.48(7)	O(22)−Mn(6)−O(16)	97.56(7)
O(6)−Mn(3)−O(9)	175.28(7)		

correction of the X-ray data by SQUEEZE is 116 e/cell, and the required value is 88 e/cell. Non-hydrogen atoms in all structures were refined with anisotropic displacement coefficients except for the two CH_2 and Me groups belonging to the amine ligand coordinated to the divalent Mn(3) atom in complex **1a**. These groups are disordered over two positions in a ratio of 41:59 and were refined with isotropic thermal parameters. The hydrogen atoms in all of the complexes were treated as idealized contributions. All software and sources of scattering factors are contained in the SHELXTL (5.10) program package (G. Sheldrick, Bruker XRD, Madison, WI).

Results and Discussion

Description of the Structures. Figure 1 shows an ORTEP illustration of complexes **1** and **3**. Selected bond distances and angles are given in Tables 3 and 4 for complex **1** and in Tables 5 and 6 for complex **3**. Complex **1** crystallizes in the $P\bar{1}$ space group. The crystal structure of **1** consists of centrosymmetrical $[Mn_{12}]$ structural units each possessing a wheel-shaped topology. Figure 2 shows a simplified view of the wheel Mn−O−Mn connectivity. The Mn atoms are ligated by acetate and the deprotonated alcohol amine ligand $mdea^{2-}$. These acetate and alkoxide moieties act as bridges between Mn atoms and are the backbone of the wheel. Complex **1** is mixed valent possessing six Mn^{II} and six Mn^{III} ions that alternate around the wheel. Atoms Mn(2), Mn(4), and Mn(6) (and symmetry-related Mn(2a), Mn(4a), and Mn(6a)) have been determined to be trivalent from their Jahn−Teller distorted geometries. These atoms exhibit Jahn−Teller elongation axes with two bond lengths that are significantly longer (e.g., 2.1989(17)−2.311(2) Å for Mn(2)) than the other four bonds (1.8890(17) and 1.9015(17) Å for Mn(2)). As shown in Figure 3, four of these Jahn−Teller elongation axes (Mn(2), Mn(2a), Mn(4), and Mn(4a)) are oriented virtually parallel to one another and orthogonal to the average plane of the $[Mn_{12}]$ ring. The Jahn−Teller elongation axes of Mn(6) and Mn(6a) orient virtually in the plane of the ring. The same situation is observed for complexes **1a**, **3**, and **3a**. Atoms Mn(1), Mn(3), and Mn(5) and the symmetry equivalent Mn(1a), Mn(3a), and Mn(5a) are divalent having bond lengths spanning a much more restricted range (e.g., 2.0972(18)−2.2502(18) Å for Mn(5)). Divalent atoms Mn(3) and Mn(3a) are seven coordinate. Complex **1a** is chemically equivalent to complex **1** except for the manner of crystallization. Complex **1a** crystallizes in the $P2_{1/n}$ space group. Also, complex **1a** does not crystallize with any solvate molecules. Figure 4 gives packing diagrams for both complex **1** (upper plot) and complex **1a** (lower plot). Complex **1** packs with each of its $[Mn_{12}]$ units oriented in the same direction. There are, however, two orientations of the $[Mn_{12}]$ units for complex **1a**. The plane of the Mn_{12} wheel for each of these two orientations is tipped ca. 30° from each other. Stacks of the $[Mn_{12}]$ units propagate in the crystallographic *a* direction for complex **1a**. The $[Mn_{12}]$ units are in close proximity to each other for complex **1a**. The nearest intermolecular distance of 6.717 Å is between Mn(6) of one $[Mn_{12}]$ unit and the Mn(1) atom of a neighboring $[Mn_{12}]$ unit. The $[Mn_{12}]$ units in complex **1** are more separated having a nearest intermolecular distance of 7.013 Å for an analogous pathway (Mn(5)−Mn(4)). Complexes **3** and **3a** are structurally similar to complexes **1** and **1a** with one notable exception. As shown in Figure 2, complex **3** differs from complex **1** in the connectivity of two μ_3-O carboxylate ligands bridging the manganese atoms. In complex **1**, O(15) of the acetate ligand has μ_3 coordination and bridges the two manganese atoms, Mn(5) and Mn(6). In complex **3**, O(16) bridges the manga-

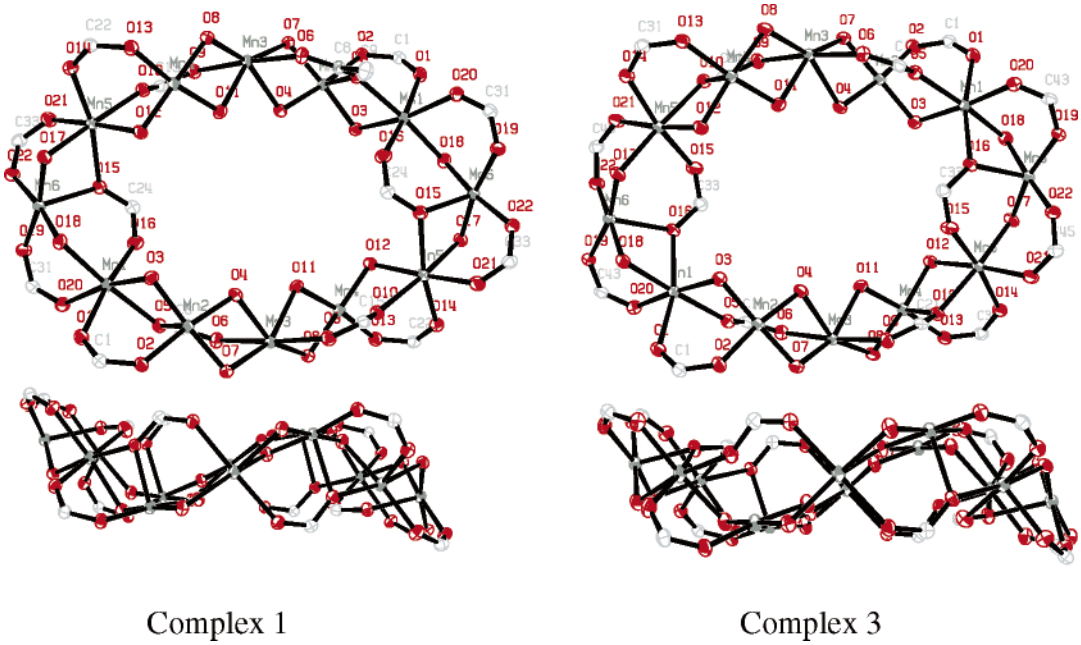

Figure 2. ORTEP diagrams of complexes **1** (left) and **3** (right) emphasizing the Mn−O−Mn connectivity. The lower plots show a side view of the wheel. For clarity, all amine ligands have been omitted.

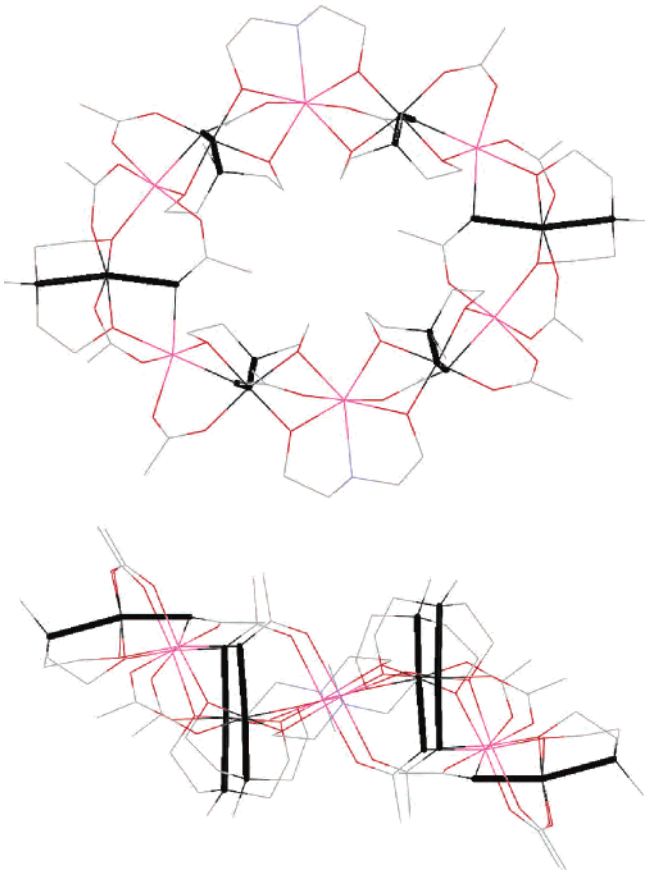

Figure 3. Illustration of complex **1** viewed orthogonal to the plane of the ring (upper plot) and a side view of the ring (lower plot). The directions of the Jahn−Teller elongation axes at Mn^{III} sites are colored black.

nese atoms Mn(6) and Mn(1). Complexes **3** and **3a** differ in the conformation of the *N*-butyl alkyl chain of the $bdea^{2-}$ ligands.

Figure 5 shows the packing diagrams of complexes **3** and **3a**. The packing of complex **3** differs from that of complex

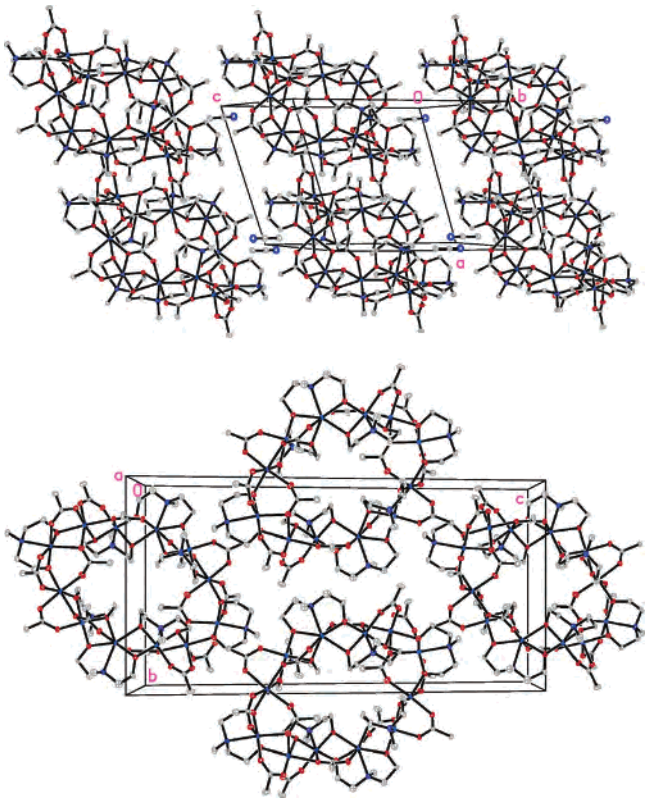

Figure 4. Packing diagrams for complex **1** (top) and complex **1a** (bottom).

3a. Complex **3a** crystallizes in the $P\bar{1}$ space group and packs with one $[Mn_{12}]$ molecule in the unit cell. The complex does not crystallize with any solvate molecules. The $[Mn_{12}]$ molecules are oriented in the same direction. Complex **3** crystallizes in a $C_{2/c}$ space group and packs with four $[Mn_{12}]$ molecules in each unit cell. There are three acetonitrile solvate molecules per each $[Mn_{12}]$ molecule. The nearest intermolecular distance between the methyl group of the *n*-butyl ligand and the methyl group of a neighboring acetate

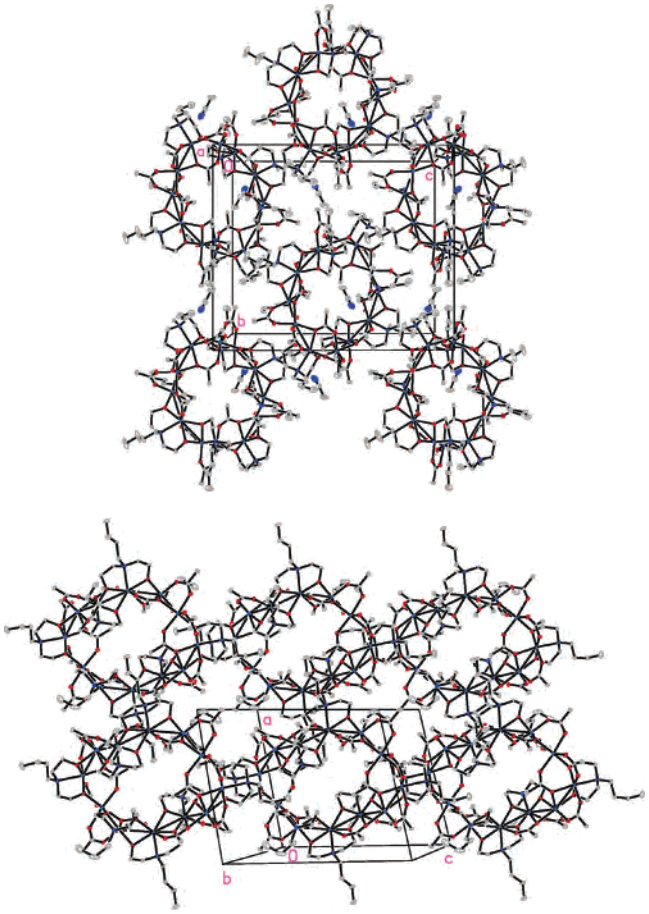

Figure 5. Packing diagrams for complex **3** (top) and complex **3a** (bottom).

ligand was found to be 3.9 Å along the *a* direction. In complex **3**, there are two orientations of the [Mn_{12}] molecules. The nearest intermolecular distance of 7.459 Å is between Mn(6) of one [Mn_{12}] unit and the Mn(6) atom of a neighboring [Mn_{12}] unit for complex **3**. The [Mn_{12}] units in complex **3** are slightly more separated, having a nearest intermolecular distance of 7.660 Å for an analogous pathway (Mn(6)−Mn(6)) between wheels.

Despite being rings, complexes **1**−**3** do not have a sufficiently large enough pore size to encapsulate a guest. In Figure 6, the space filling diagrams for complexes **1** and **3** are shown. In complexes **1** and **3**, the methyl or *n*-butyl "arm" of the diethoxide amine ligand covers the pore preventing a potential guest from entering.

Table 7. Solution ^{1}H NMR Spectral Data for Complexes $[Mn_{12}(mdea)_8(O_2CCH_3)_{14}]\cdot CH_3CN$ (**1**) and $[Mn_{12}(edea)_8(O_2CCH_3)_{14}]$ (**2**)

complex	peak (δ)	integration	assignment	label
1	4.18	4.0	CH_2	f
	2.74	4.0	CH_2	g
	2.43	3.0	CH_3	h
	1.17−0.82	5.2	CH_3acetate	i
	1.94		CH_3CN	S
2	4.12	4.0	CH_2	a
	2.71	3.9	CH_2	b
	2.16	2.0	CH_2	c
	1.18	3.0	CH_3	d
	0.98	5.3	CH_3acetate	e
	1.94		CH_3CN	S

^{1}H NMR Spectroscopy. ^{1}H NMR data were collected for complexes **1** and **2** to examine their structure and stability in solution (Table 7). Figure 7 gives the room-temperature spectra collected at 300 MHz in $CDCl_3$ for complexes **1** and **2**. Peak assignments were made on the basis of the integrations. Strong broad peaks associated with the methylene and methyl groups of the *N*-methyldiethoxide (**1**) or *N*-ethyldiethoxide (**2**) amine ligands are observed. The strong peak at 1.94 ppm is from the acetonitrile with which complexes **1** and **2** cocrystallize. The X-ray structures show that there are three pairs of equivalent Mn^{III} ions and three pairs of equivalent Mn^{II} atoms. Four of the diethoxide amine ligands are coordinated to Mn^{II} atoms, while the other two are coordinated to Mn^{III} atoms. Only one grouping of resonances belonging to the diethoxide amine ligand is observed. A series of weak broad peaks in the 3−4 ppm region are present for complexes **1** and **2**.

DC Magnetic Susceptibility Studies. Figure 8 illustrates the variable-temperature magnetic susceptibility data measured from 300 to 2 K with an applied field of 1 T for complexes **1**, **2**, and **3**. Upon cooling, the value of $\chi_M T$ decreases from 39.7 cm^3 K mol^{-1} at 300 K to a plateau value of ∼39 cm^3 K mol^{-1} at 160 K for complex **1**, below which it slowly decreases to a value of 22.8 cm^3 K mol^{-1} at 20 K. Below 20 K, $\chi_M T$ sharply decreases to a value of 9.7 cm^3 K mol^{-1} at 2 K. This sharp decrease is caused by the zero-field splitting of the spin ground state. The $\chi_M T$ value of 39.7 cm^3 K mol^{-1} at 300 K is smaller than the theoretical spin only value of 44.26 cm^3 K mol^{-1} for six Mn^{II} and six Mn^{III} noninteracting ions. The value of the product $\chi_M T$ slowly decreases with decreasing temperature, indicating weak antiferromagnetic magnetic exchange interactions. As

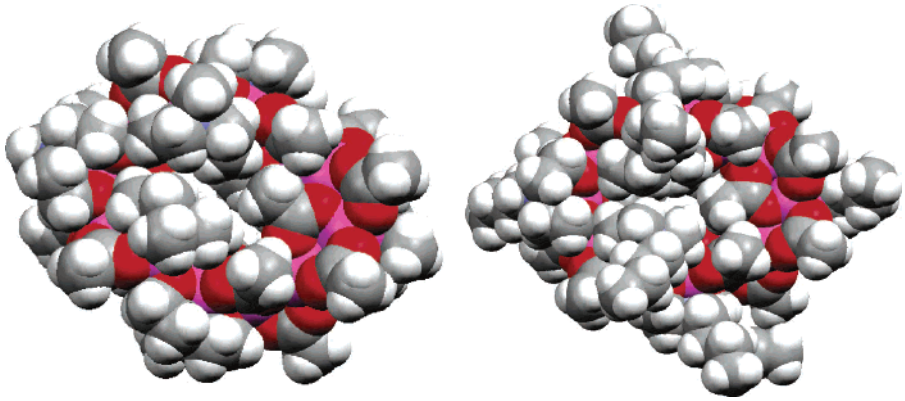

Figure 6. Space filling illustration of complexes **1** (left) and **3**. The solvate molecules have been omitted for clarity.

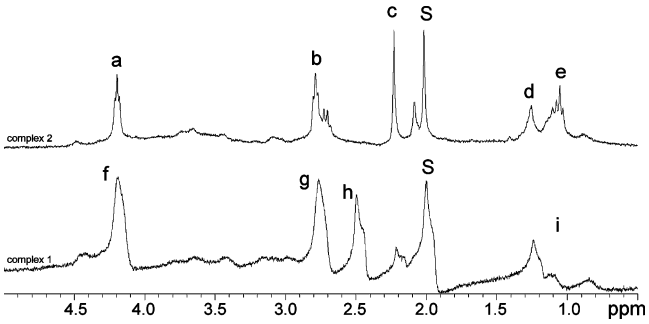

Figure 7. Solution ($CDCl_3$) ^1H NMR (300 MHz) spectra of complexes **2** (top trace) and **1** (bottom trace).

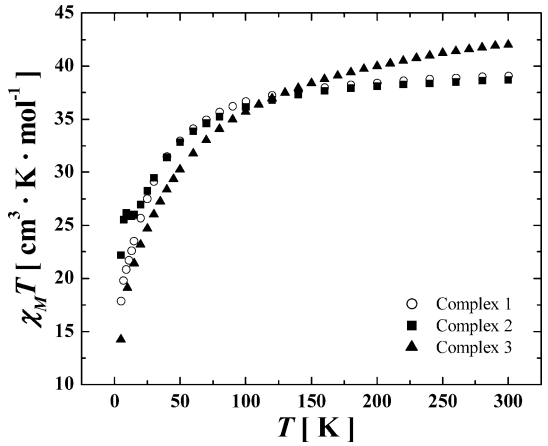

Figure 8. Plot of $\chi_M T$ versus temperature for complexes **1** (○), **2** (■), and **3** (▲). χ_M is the molar susceptibility. The data were collected with an applied field of 1 T.

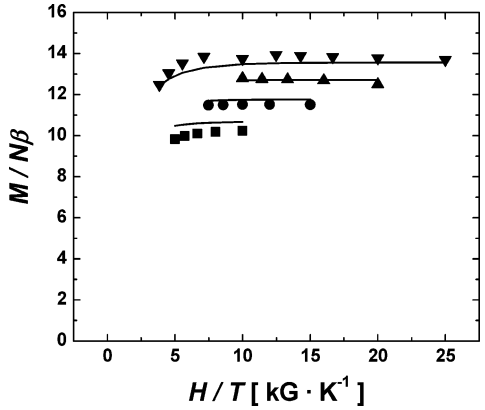

Figure 9. Plot of the reduced magnetization ($M/N\beta$), where M is the molar magnetization, N is Avogadro's number, and β is the Bohr magneton, versus H/T for complex **1**. Data were collected at 5 (▼), 4 (▲), 3 (●), and 2 T (■) in the temperature range of 2.0−13 K. The solid line represents the least-squares fit of the data with the parameters $S = 8$, $g = 2.0$, and $D = -0.47$ cm^{-1}. See the text for the details of this analysis.

can be seen in Figure 8, complex **2** exhibits a response similar to that of complex **1**. Since the yield of complex **3a** was very low, magnetic susceptibility studies were carried out on complex **3** only. For complex **3**, as the temperature decreases, the value of $\chi_M T$ decreases from 42.3 cm^3 K mol^{-1} at 300 K to 14.3 cm^3 K mol^{-1} at 5 K . The $\chi_M T$ value of 42.3 cm^3 K mol^{-1} is slightly lower than the spin only value of 44.26 cm^3 K mol^{-1} for six spin only noninteracting Mn^{II} and six Mn^{III} atoms.

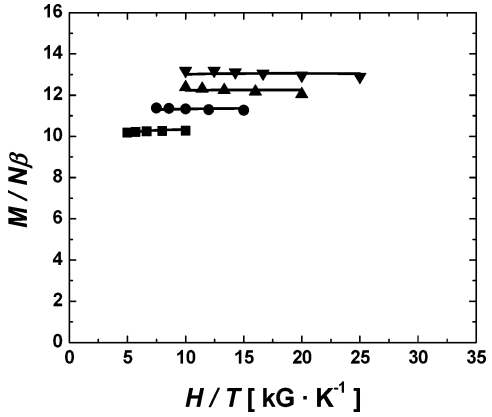

Figure 10. Plot of the reduced magnetization ($M/N\beta$), where M is the molar magnetization, N is Avogadro's number, and β is the Bohr magneton, versus H/T for complex **2**. Data were collected at 5 (▼), 4 (▲), 3 (●), and 2 T (■) in the temperature range of 2.0−30.0 K. The solid line represents the least-squares fit of the data with the parameters $S = 8$, $g = 2.0$, and $D = -0.49$ cm^{-1}. See the text for the details of this analysis.

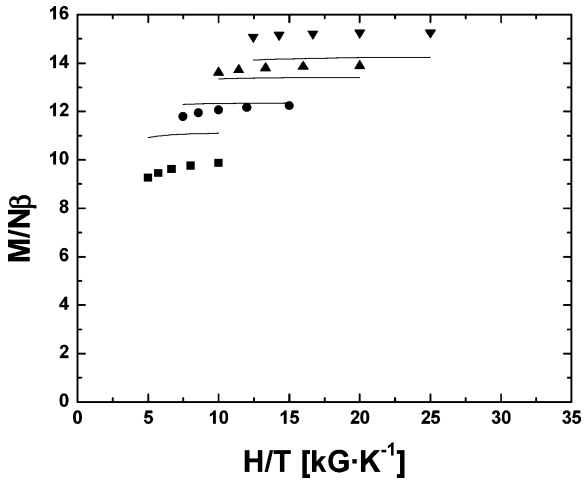

Figure 11. Plot of the reduced magnetization ($M/N\beta$), where M is the molar magnetization, N is Avogadro's number, and β is the Bohr magneton, versus H/T for complex **3**. Data were collected at 5 (▼), 4 (▲), 3 (●), and 2 T (■) in the temperature range of 2.0−30.0 K. The solid line represents the least-squares fit of the data with the parameters $S = 8$, $g = 2.0$, and $D = -0.37$ cm^{-1}. See the text for the details of this analysis.

To determine the spin ground states of complexes **1**, **2**, and **3** variable-field magnetization data were collected over several fields down to the lowest temperature of 1.8 K and are depicted in Figure 9 for complex **1**, Figure 10 for complex **2**, and Figure 11 for complex **3**. Nonsuperimposable isofields were observed and suggest that complexes **1** and **2** possess significant zero-field splitting in their ground states. Theoretical magnetizations were calculated by means of a full matrix diagonalization (employing a powder average of Gaussian quadrature) of eq 1. The spin Hamiltonian used for an $S = 8$ ground state which included the Zeeman interaction and axial second-order zero-field splitting, $D\hat{S}_Z^2$, is represented in eq 1.

$$\hat{H} = \mu_B g H \hat{S} + D\left[\hat{S}_Z^2 - \frac{1}{3}S(S+1)\right] \qquad (1)$$

The calculated magnetizations were least-squares fit to the experimental data collected in the temperature range of 2−13 K for complex **1** and 2−5 K for complexes **2** and **3**.

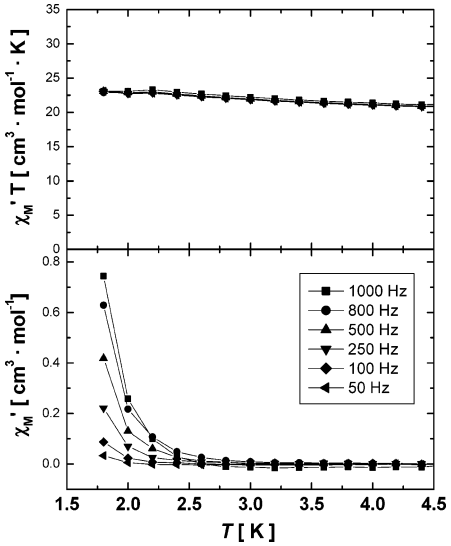

Figure 12. Plot (upper) of $\chi'_M T$ versus temperature where χ'_M is the molar in-phase ac susceptibility for complex **1**. The lower plot shows the χ''_M versus temperature where χ''_M is the molar out-of-phase ac susceptibility. The data were collected with a 3 G ac field oscillating at frequencies of 1000 (■), 500 (●), and 50 (▼) Hz.

Restriction of the temperature range was necessary to yield values of g that are reasonable for a mixed valent $Mn^{III}Mn^{II}$ system. A minimum was found with the spin Hamiltonian parameters $S = 8$, $g = 2.0$, and $D = -0.47$ cm^{-1} for complex **1**; $S = 8$, $g = 2.0$, and $D = -0.49$ cm^{-1} for complex **2**; and $S = 8$, $g = 2.0$, and $D = -0.37$ cm^{-1} for complex **3**. The solid lines shown in Figures 9−11 represent the theoretical least-squares fits. It is not clear why a fit of comparable quality to those acquired for complexes **1** and **2** could not be obtained for the data collected for complex **3** (Figure 11).

AC Magnetic Susceptibility Studies. The ac magnetic susceptibility data were collected in zero-applied dc field. Figure 12 (upper) depicts the temperature dependence of the in-phase ac susceptibility, $\chi'_M T$, collected with a 3 G ac field oscillating at frequencies in the range of 1000−50 Hz for complex **1** in the temperature range of 1.8−10 K. The product $\chi'_M T$ collected at 1000 Hz slowly diminishes from a value of 21.2 cm^3 K mol^{-1} at 10 K to a minimum of 20.7 cm^3 K mol^{-1} at 7 K. Below 7 K, the value of $\chi'_M T$ for complex **1** steadily increases to a maximum of 23.31 cm^3 K mol^{-1} at 2.2 K. The value of $\chi'_M T$ at the lowest temperatures, 1.8, 2.0, and 2.2 K, exhibits a small frequency dependence. Figure 13 depicts the temperature dependence of both the in-phase, $\chi'_M T$, and out-of-phase ac susceptibility, χ''_M, collected with several 3 G oscillating ac fields for complex **2**. The in-phase ac susceptibility data for both complexes **1** and **2** are consistent with the dc susceptibilities (e.g., $\chi'_M T$ (1000 Hz) = 26.57 cm^3 K mol^{-1} and $\chi_M T$ = 22.21 cm^3 K mol^{-1} at 5 K for complex **2** and $\chi'_M T$ (1000 Hz) = 20.71 cm^3 K mol^{-1} and $\chi_M T$ = 18.81 cm^3 K mol^{-1} at 5 K for complex **1**). Figure 14 shows the ac data for complex **3** in zero-applied dc field. The upper plots depicts the temperature dependence of the in-phase ac susceptibility at frequencies ranging from 997 to 250 Hz within a temperature range of 4.5−1.8 K collected in a 3 G ac field. The $\chi'_M T$ value decreases from 14.4 cm^3 K mol^{-1} at 4.5 K to 10.7 cm^3 K mol^{-1} at 1.8 K.

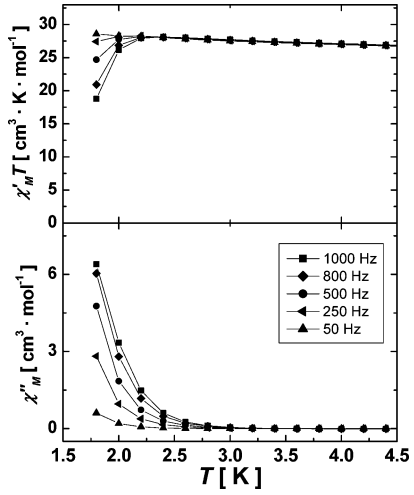

Figure 13. Plot (upper) of $\chi'_M T$ versus temperature where χ'_M is the molar in-phase ac susceptibility for complex **2**. The lower plot shows the χ''_M versus temperature where χ''_M is the molar out-of-phase ac susceptibility. The data were collected with a 3 G ac field oscillating at frequencies of 1000 (■), 500 (●), and 50 (▼) Hz.

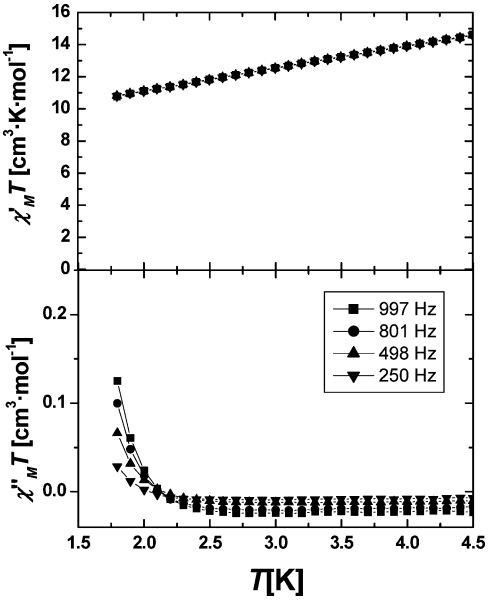

Figure 14. Plot (upper) of $\chi'_M T$ versus temperature where χ'_M is the molar in-phase ac susceptibility for complex **3**. The lower plot shows the χ''_M versus temperature where χ''_M is the molar out-of-phase ac susceptibility. The data were collected with a 3 G ac field oscillating at frequencies of 1000 (■), 500 (●), and 50 (▼) Hz.

Each of the [Mn_{12}] wheel-shaped complexes, **1**, **2**, and **3**, exhibits a frequency-dependent out-of-phase component to their ac susceptibility response below 2.6 K, as seen in the lower portions of Figures 12−14. This frequency-dependent response indicates that there are slow kinetics of magnetization reversal relative to the frequency of the oscillating ac field and is often associated with the phenomenon of single-molecule magnetism.[23] The out-of-phase peak for complex **3** grows in at a lower temperature than the peaks observed for complexes **1** and **1a** and is a consequence of the smaller

(23) Christou, G.; Gatteschi, D.; Hendrickson, D. N.; Sessoli, R. *MRS Bull.* **2000**, *25*, 66.

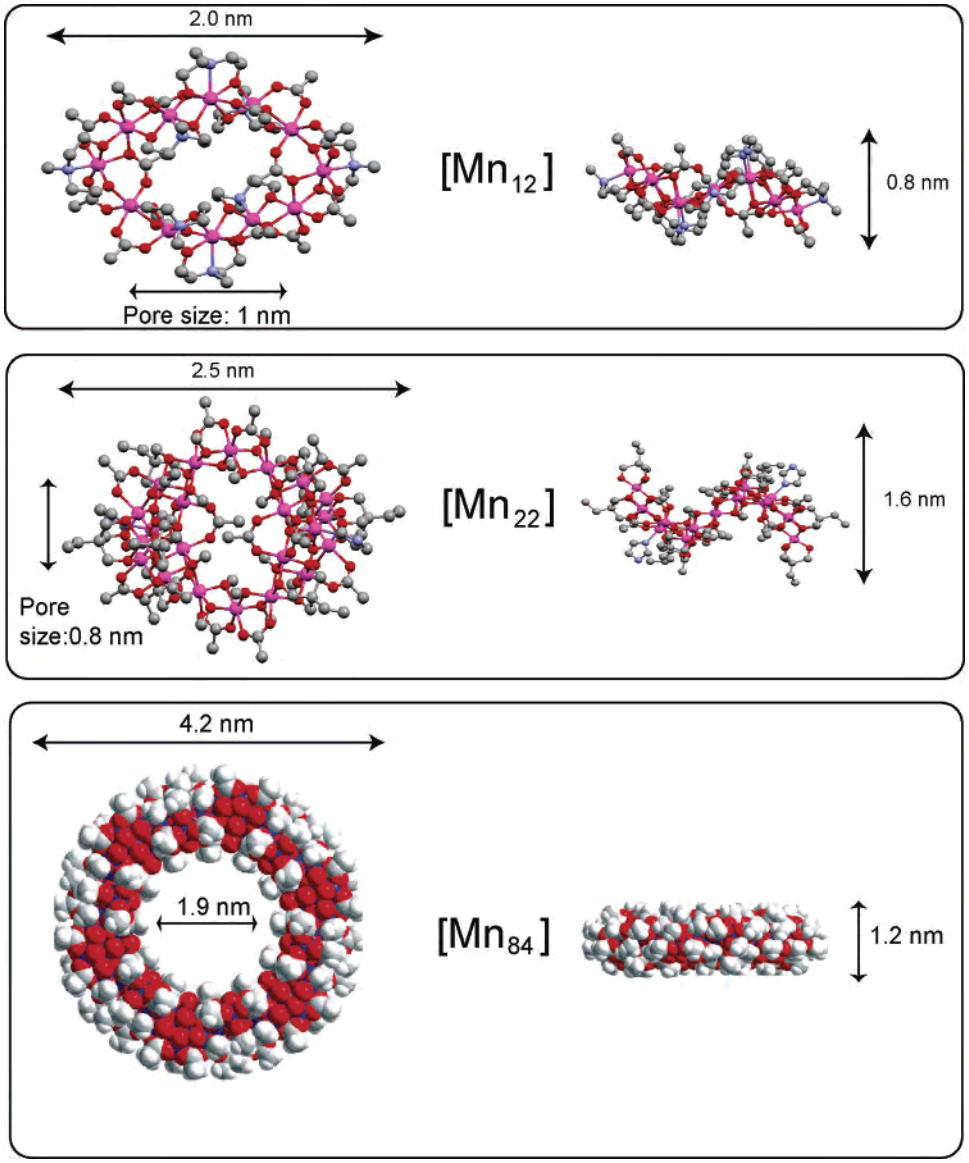

Figure 15. Structures and nanoscale dimensions of complex **1** (upper plot), [Mn_{22}] (middle plot), and [Mn_{84}] (lower plot). For clarity, the relative sizes of the complexes are not drawn to scale.

D value of complex **3** relative to that of complexes **1** and **2**. A full peak is not observable in the accessible temperature ranges; the lowest obtainable temperature is 1.8 K. Given that complexes **1**, **2**, and **3** have the high-spin ground states of $S = 8$ as well as *negative* magnetic anisotropy, indicated by a zero-field splitting *D* value of -0.47 cm^{-1} for complex **1**, $D = -0.49$ cm^{-1} for complex **2**, and $D = -0.37$ cm^{-1} for complex **3**, it is likely that all of the complexes studied are single-molecule magnets.

Conclusions

Although all three complexes have an even number of antiferromagnetically coupled spin carriers, each complex, **1**, **2**, and **3**, has a non-zero-spin ground state of $S = 8$. The magnetic exchange interactions between the $Mn^{III}-O-Mn^{II}$ units are not the same for each $Mn^{III}-Mn^{II}$ pair going around the wheel structure. Complexes **1**, **2**, and **3** are not circles and can be described as ellipses. Since the bond distances and angles are different for any given position within the wheel for a $Mn^{III}-O-Mn^{II}$ pair, the magnetic exchange interactions between Mn atoms are not uniformly the same. It is likely that the magnetic exchange interactions between three Mn atoms (e.g., Mn(5a), Mn(1), and Mn(6a) for complex **1** (Figure 1)) create a spin-frustrated subunit for the [Mn_{12}] wheels. These competing antiferromagnetic exchange interactions between the Mn^{III} and Mn^{II} atoms yield a ground state that is larger than the fully spin-coupled $S = 3$ state that would be expected for an antiferromagnetic system comprised of six Mn^{III} and six Mn^{II} atoms.

Loss et al.[9,12] outlined several requirements to observe coherent magnetization tunneling in antiferromagnetic rings. The first requirement is that the wheel has a non-zero-spin ground state. A second requirement is that each wheel should be spatially or chemically separated from its neighbor to prevent it from interacting with dipolar magnetic fields. A third requirement calls for the minimization of internal sources of magnetic fields within the molecule, such as the hyperfine fields of the nuclear spins of the atoms making

up the wheel. Complexes **1**, **2**, and **3** satisfy the first requirement since each has an $S = 8$ ground state. However, complexes **1**, **1a**, **3**, and **3a** have close intermolecular contact (nearest Mn−Mn distance between wheels: 6.717 Å for **1a**, 7.013 Å for **1**, 7.459 Å for **3**, and 7.660 Å for **3a**) with their neighbor [Mn_{12}] wheels within a crystal. The Mn nuclei in complexes **1**, **2**, and **3** also have a nuclear spin of $I = 7/2$.

In conclusion, the syntheses and crystal structures of new [Mn_{12}] complexes with a wheel-shaped topology are reported. These new [Mn_{12}] wheel complexes, **1**, **2**, and **3**, are single-molecule magnets. Complexes **1a** and **3a** represent two different crystallographic phases that have been isolated for complexes **1** and **3**. Magnetometery experiments confirm that these complexes have a high-spin ground state of $S = 8$. A frequency-dependent out-of-phase response in ac susceptibility data is observed indicating that there are slow kinetics of magnetization reversal. A ligand system has also been identified that gives [Mn_{12}] wheel structures from different starting materials. These [Mn_{12}] complexes are a welcome addition to a small but growing series of Mn-based wheel-shaped complexes. Figure 15 shows the [Mn_{12}] wheel complex along with the two other Mn-based wheel SMM complexes, [Mn_{22}][24] and [Mn_{84}].[7] The nanoscale dimensions of these three complexes are shown. The [Mn_{12}] and [Mn_{22}] complexes are roughly the same size. The [Mn_{84}] SMM is the largest wheel but has the smallest spin ground state ($S = 6$) of the wheel complexes.

Acknowledgment. This work was supported by the National Science Foundation.

Supporting Information Available: X-ray crystallographic files in CIF format are available for complexes **1**, **1a**, **3**, and **3a**. This material is available free of charge via the Internet at http://pubs.acs.org.

IC048316L

(24) Murugesu, M.; Raftery, J.; Wernsdorfer, W.; Christou, G.; Brechin, E. K. *Inorg. Chem.* **2004**, *43*, 4203.

(25) Note added in Proof: Complex **1** has recently been reported by others. Foguet-Albiol, D.; O'Brien, T. A.; Wernsdorfer, W.; Moulton, B.; Zaworotko, M.; Abboud, K. A.; Christou, G. *Angew. Chem., Int. Ed.* **2005**, *44*, 897.